PCCP

The mechanism of the reaction FH + $H_2C{=}CH_2$ → $H_3C{-}CFH_2$. Investigation of hidden intermediates with the unified reaction valley approach†‡

Dieter Cremer,* Anan Wu and Elfi Kraka

Department of Theoretical Chemistry, Göteborg University, Reutersgatan 2, S-41320 Göteborg, Sweden

Received 22nd September 2000, Accepted 27th November 2000
First published as an Advance Article on the web 22nd January 2001

The unified reaction valley approach (URVA) is used to investigate the mechanism of the reaction $H_2C{=}CH_2$ + FH → $H_3C{-}CH_2F$ (reaction I) at different levels of theory (HF, MP2 and CCSD(T)) with different basis sets (6-31G(d,p), 6-311++G(3df,3dp) and cc-pVTZ). URVA is based on the reaction path Hamiltonian, the intrinsic reaction coordinate, and the characterization of normal modes, reaction path vector and curvature vector in terms of generalized adiabatic modes associated with internal parameters that are used to describe the reaction complex. In addition, URVA combines the investigation of the harmonic reaction valley with the analysis of attractive and repulsive forces exerted on the nuclei by analyzing the changes of the electron density distribution along the reaction path. It is shown that reaction I involves two different chemical processes: (a) the simultaneous FH bond cleavage and CH bond formation leading to an intermediate structure with ion-pair character and (b) the formation of a CF bond and, by this, the final product. The properties of the reaction complex suggest the possibility that a hidden intermediate formed in process (a), which upon a change in the reaction conditions (environment, substitution pattern) can convert into a real intermediate (in solution: solvated ion pairs). Using the results of the URVA analysis of reaction I predictions with regard to the occurrence of hidden intermediates in related addition/cycloaddition reactions are made.

1 Introduction

In recent work, we described the unified reaction valley approach (URVA),[1,2] which is based on the reaction path Hamiltonian (RPH),[3] the intrinsic reaction coordinate (IRC)[4] and the generalized adiabatic mode concept.[5,6] URVA was developed to obtain a detailed description of the changes in the physical and chemical properties of a reaction complex (RC, the supermolecule made up from the reacting molecules) along the reaction valley that connects the stationary points associated with reactants, transition state (TS) and products. URVA can be used to elucidate the mechanism of a chemical reaction and to get information on its reaction dynamics.[1,2] The present work is part of a larger research project intended to investigate the difference between symmetry-allowed and symmetry-forbidden concerted reactions utilizing URVA. As was demonstrated by Woodward and Hoffmann,[7] symmetry-forbidden reactions are energetically unfavorable because of a symmetry-induced reaction barrier that enhances the electronically-induced barrier value. This is the basis for the Woodward–Hoffmann rules for pericyclic concerted reactions,[7] which predict that symmetry-forbidden reactions proceed slower than allowed reactions. However, beside the qualitative difference in activation energies there should be also a difference in the reaction mechanism. For example, it is known that symmetry-forbidden reactions can avoid the unfavorable high energy concerted reaction path by choosing a nonconcerted path *via* an intermediate.[8,9] This, of course will lead to a different stereochemistry of the reaction and, by this, often to different products. The reaction we investigated in this work is the addition of FH (**1**) to ethene (**2**) (henceforth called reaction I, see Scheme 1), which is a representative of a large class of addition reactions involving unsaturated hydrocarbons and the molecules H–X, X–X (X = H, halogen, BH_2, NH_2, OH, *etc.*) or X=X (X = CH_2 NH, O, *etc.*).[10] Quantum chemical investigations suggest that reaction I proceeds in three steps:[11–19]

The reactants **1** and **2** form first the C_{2v}-symmetrical van der Waals complex **3** (Scheme 1), for which conclusive evidence has been gathered by both theory[12–19] and experiment[20] that concern directly complex **3** or closely related complexes.[21–25] Rotation of **1** within the heavy atom plane and breaking of C_{2v}-symmetry leads to the four-

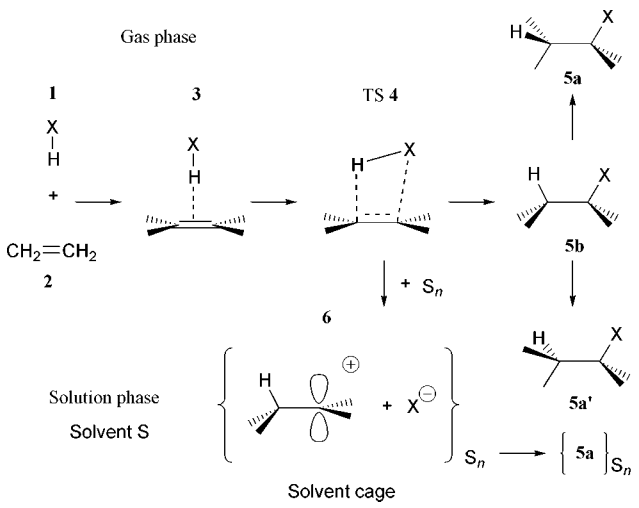

Scheme 1

† Presented at the Third European Conference on Computational Chemistry, Budapest, Hungary, September 4–8, 2000.
‡ Dedicated to Professor Marianne Baudler on the occasion of her 80th birthday.

 DOI: 10.1039/b007733j

centered transition state (TS) **4** and the addition-product fluoroethane **5**. The reaction path bifurcates in the exit channel, which corresponds to a left- or right-rotation at the newly formed CC single bond, so that **5** is formed in its more stable staggered form **5a** rather than the eclipsed form **5b**[26] (Scheme 1). The energetics for the reverse reaction (elimination of **1** from **5** by pyrolysis) was measured.[27,28] Hence, the basic features of the mechanism of reaction I are well known.[11–28] An early very detailed description of the mechanism of reaction I was obtained by Kato and Morokuma, who pioneered the use of the RPH for a specific chemical problem.[11] Independent and parallel to the more general formulation of the RPH by Miller, Handy and Adams,[3] these authors developed methods to study the reverse reaction I in a short range close to the TS, focusing on energy transfer and energy dissipation. Although the investigation had to be limited to Hartree–Fock (HF) calculations with the 4-31G basis set, essential tools for a better understanding of the reaction mechanism were worked out to adequately describe the possibility of rate enhancement by mode-selective excitation of vibrational modes.[11] In this work, we will use reaction I as a simple example for a concerted symmetry-forbidden reaction involving a polar reaction partner. It is known that HX–alkene addition reactions can proceed with a different mechanism in solution, leading to ion pair intermediates.[8–10] Changes in the mechanism result, in particular, in the presence of catalysts[8,9,29] where even a second HX molecule can have strong catalytic effects as was demonstrated by Bertran and others.[30–33] *Ab initio* investigations on addition reactions showed also that by varying the reaction partners the mechanism shown in Scheme 1 may change in the gas phase.[33–36] Although we will focus on the mechanism of I as sketched in Scheme 1, results obtained in this investigation will enable us to link various mechanisms to a general reaction pattern for those addition/cycloaddition reactions, which are formally symmetry-forbidden. Symmetry rules apply to pericyclic reactions and considering the structure of **3** one might hesitate to speak even in the gas phase of a pericyclic reaction; however, the symmetry of **3** is broken in the reaction and addition of **1** proceeds *via* a four rather than a three-centered TS, which can be characterized as a $[\sigma^2s + \pi^2s]$ TS typical of a symmetry-forbidden reaction. In this way, reaction I is a useful model reaction for investigating (a) a non-trivial symmetry-forbidden reaction (the archetypical forbidden reaction $H_2 + H_2$ leading to H exchange[37,38] would be the corresponding trivial example) with (b) an asymmetrical TS (the formation of the new bonds does not occur simultaneously) and (c) a strong dependence on the environment. Therefore, we will investigate whether the mechanism of the gas phase reaction provides any clue as to how the reaction may proceed in a different environment. Our investigation will focus on the sequence of bond breaking and bond forming processes and the distinction of different reaction phases and their location along the reaction path. A general mechanistic description will be derived by relating typical changes in the electronic structure of the RC to the changes in its geometry and the forces acting on its atoms. We will show that beside the stationary points along the reaction path there are structures of the RC that play an important role for the mechanism. In this connection, we will introduce the notion of a *hidden intermediate*, which is a transient structure found along the reaction path with unique electronic and structural features but which does not occupy a distinct stationary point on the potential energy surface (PES). Hence, a hidden intermediate does not represent a unique chemical entity (located at a stationary point) in the mechanism under investigation, but it can become one as a result of environmental changes or changes in the substituents, *i.e.* it is the mechanistic link between different reaction mechanisms observed under different environmental conditions or substitution patterns. We will investigate for which addition/cycloaddition reactions hidden intermediates can be expected and how a knowledge and description of hidden intermediates enables one to predict mechanistic changes. Results of this work will be presented in three sections. In section 2, we will briefly describe the theory of URVA and the computational methods used. In section 3, the reaction path and reaction valley of reaction I will be described. This is followed by a mechanistic discussion in section 4.

2 Theory and computational methods

URVA[1,2] is based on a partitioning of $3K - L$-dimensional space (L: number of overall rotations and translations, K: number of atoms in the RC) of the RC into a one-dimensional reaction path space, along which the translational motion of the RC takes place, and a $(3K - L) - 1$-dimensional orthogonal space, in which the transverse vibrations of the RC orthogonal to the reaction path movement occur. In other words, one distinguishes between the path along the valley floor and the shape of the valley in the transverse directions when following the reaction path from reactants to products.

The quantities used for describing reaction path and reaction valley are listed in Table 1. Their calculation was discussed in previous work[1–4,39] and, therefore, only some basic definitions are given, which are essential for the discussion. The reaction path used in connection with the RPH is the steepest descent path in mass-weighted coordinates.[3] It is

Table 1 Symbols and quantities used

Symbol	Property and comment
General	
$\boldsymbol{x}_i$	Cartesian coordinate
$\boldsymbol{x}_i$	Mass weighted $\boldsymbol{x}_i$
q_n	Internal coordinates: bond length *Rn*, bonding angle *An*, dihedral angle *Dn*
ξ_n	Geometrical parameter such as symmetry coordinate, internal coordinate q_n, *etc.*
$\boldsymbol{l}_\mu$	Normal mode vector
$\boldsymbol{a}_n$	Adiabatic internal mode (AIM) vector associated with q_n
$\boldsymbol{M}$	Mass matrix
Reaction path	
$\tilde{\boldsymbol{x}}(s)$	Reaction path
s	Reaction path length
$V(s)$	Classical potential along the reaction path
$\boldsymbol{t}(s)$	Reaction path vector, direction of reaction path
$\boldsymbol{u}_n(s)$	Internal coordinate mode vector (associated with q_n) for the motion along the reaction path
$A_{n,s}(t; s)$	Amplitude of internal coordinate mode $\boldsymbol{u}_n$
$k(s)$	Curvature vector
$\kappa(s)$	Scalar curvature of reaction path, length of curvature vector
Reaction valley	
$\tilde{\boldsymbol{l}}^{\mathrm{s}}_\mu(s)$	Generalized (mass-weighted) normal mode vector
$\boldsymbol{Q}^{\mathrm{g}}_\mu(s)$	Generalized normal mode coordinate
$\omega^{\mathrm{g}}_\mu(s)$	Frequency of generalized normal mode (harmonic approach)
k^{g}_μ	Force constant of generalized normal mode
$\boldsymbol{a}^{\mathrm{g}}_n(s)$	Generalized adiabatic internal mode
$k^a_n(s)$	Force constant of generalized AIM $\boldsymbol{a}^{\mathrm{g}}_n(s)$
$m^a_n(s)$	Mass associated with generalized AIM $\boldsymbol{a}^{\mathrm{g}}_n(s)$
$\omega^a_n(s)$	Frequency of generalized AIM $\boldsymbol{a}^{\mathrm{g}}_n(s)$
$V(s, \boldsymbol{Q})$	Harmonic reaction valley
$B_{\mu s}(s)$	Normal mode curvature coupling coefficients (energy transfer)
$B_{\mu\nu}(s)$	Coriolis (mode–mode) coupling coefficients (energy dissipation)
$A_{n s}(\boldsymbol{k}, s)$	Adiabatic mode curvature coupling coefficients (decomposition of curvature into AIM contribution)

defined by the line $\tilde{\boldsymbol{x}}(s)$, which is given as a column vector with $3K$ mass-weighted Cartesian coordinates $\boldsymbol{x}_i$. We will use the tilde throughout this work to indicate mass-weighting. The reaction path is given parametrically in terms of its arc length s defined by the differential

$$\mathrm{d}s^2 = \mathrm{d}\boldsymbol{x}^\dagger \boldsymbol{M} \mathrm{d}\boldsymbol{x} = \mathrm{d}\tilde{\boldsymbol{x}}^\dagger \mathrm{d}\tilde{\boldsymbol{x}} \tag{1}$$

with $\boldsymbol{M}$ being the diagonal matrix of nuclear masses. The direction of the reaction path $\tilde{\boldsymbol{x}}(s)$ is determined by the reaction path vector $\boldsymbol{t}(s)$ identical to the normalized energy gradient vector $\tilde{\boldsymbol{g}}(\tilde{\boldsymbol{x}}(s))$. To determine the RPH and the reaction valley, $N_{\mathrm{vib}} = (3K - L) - 1$ (nonlinear RCs: $N_{\mathrm{vib}} = 3K - 7$; linear RCs: $N_{\mathrm{vib}} = 3K - 6$) generalized normal modes $\tilde{\boldsymbol{l}}^{\mathrm{g}}_\mu(s)$ and their associated frequencies $\omega^{\mathrm{g}}_\mu(s)$ have to be calculated.[1,3,39] Then, the *harmonic* reaction valley can be described according to eqn. (2).

$$V(s, \boldsymbol{Q}) = V(s) + \frac{1}{2} \sum_{\mu=1}^{N_{\mathrm{vib}}} k^{\mathrm{g}}_\mu(s) \cdot [Q^{\mathrm{g}}_\mu(s)]^2 \tag{2}$$

where $k^{\mathrm{g}}_\mu(s)$ is the generalized normal mode force constant, $Q^{\mathrm{g}}_\mu(s)$ is the generalized normal mode coordinate and $V(s)$ the energy profile along the reaction path. The exchange of energy between the reaction path mode and transverse vibrational modes can be studied provided the curvature vector $\boldsymbol{k}(s)$, the scalar curvature $\kappa(s)$ and the curvature coupling elements $B_{\mu,s}(s)$ are known while mode–mode coupling elements $B_{\mu,\nu}(s)$ provide an insight into energy dissipation.[1–3,39–41] These quantities are defined in eqns. (3)–(6).

$$\boldsymbol{k}(s) = \mathrm{d}^2\tilde{\boldsymbol{x}}(s)/\mathrm{d}s^2 \tag{3}$$

$$\kappa(s) = [\boldsymbol{k}(s)^\dagger \boldsymbol{k}(s)]^{1/2} = \left[\sum_{\mu=1}^{N_{\mathrm{vib}}} B^2_{\mu,s}(s)\right]^{1/2} \tag{4}$$

$$B_{\mu,s}(s) = \boldsymbol{k}(s)^\dagger \tilde{\boldsymbol{l}}^{\mathrm{g}}_\mu(s) \tag{5}$$

$$B_{\mu,\nu}(s) = \tilde{\boldsymbol{l}}^{\mathrm{g}}_\mu(s)^\dagger [\mathrm{d}\tilde{\boldsymbol{l}}^{\mathrm{g}}_\mu/\mathrm{d}s] = -B_{\nu,\mu}(s) \tag{6}$$

where the curvature coupling elements $B_{\mu,s}(s)$ represent coefficients of the expansion of the curvature vector in terms of generalized normal modes. In this work, the scalar curvature $\kappa(s)$ is graphically presented to locate its maxima along the reaction path, which indicate those points on the path where energy can flow from one (or more) of the transverse normal vibrational modes into the motion along the reaction path (or *vice versa*) thus increasing (or decreasing) the reaction rate. Hence, the reaction rate can be enhanced by pumping energy (with the help of a laser) in that particular vibrational mode, which couples with the motion along the reaction path (*mode selective rate enhancement*[40]). The curvature coupling coefficients $B_{\mu,s}(s)$ of eqn. (5) determine how much energy can be retrieved from (transferred into) normal mode $\tilde{\boldsymbol{l}}^{\mathrm{g}}_\mu(s)$. Since the normal modes are delocalized, it is difficult to identify substituents or molecular fragments, which by their vibrations can be used to channel external energy *via* vibrational modes into the reaction path mode (rate enhancement) or, alternatively, are responsible for energy transfer from the reaction path mode into vibrational modes (rate reduction). Therefore, the curvature coupling coefficients $B_{\mu,s}(s)$ are expressed in terms of adiabatic internal vibrational modes (AIMs) that can be directly associated with chemically relevant molecular fragments or structural units.[1,2,5,6]

2.1 Generalized adiabatic modes

An adiabatic internal vibrational mode described by the mode vector $\boldsymbol{a}_n$ is an elementary vibrational mode associated with an internal parameter ξ_n used to describe a molecular fragment ϕ_n.[5,6] Adiabatic modes are based on a dynamic principle (leading parameter principle[5]) and are directly obtained from a modified form of the Euler–Lagrange equations.[5] They comply with the symmetry of the molecule and are independent of the composition of the set of internal parameters ξ_n (symmetry coordinates, internal coordinates, *etc.*). Furthermore, they are perfectly suited to characterize normal vibrational modes (characterization of normal modes approach)[5,6] in the common language of chemistry that attempts to express molecular properties in the form of internal parameters ξ_n such as internal coordinates q_n. The latter are used in this work as one useful choice for internal parameters ξ_n because structure and structural changes are normally discussed in terms of these coordinates. The generalized adiabatic internal mode $\boldsymbol{a}^{\mathrm{g}}_n(s)$ is expressed in $(3K - L) - 1$- rather than $3K - L$-dimensional space. Its properties are given by associated force constant $k^a_n(s)$, mass $m^a_n(s)$, and frequency $\omega^a_n(s)$ according to eqns. (7),[5,6]

$$(\boldsymbol{a}^{\mathrm{g}}_n(s))_\mu = \frac{D_{n\mu}(s)}{k^{\mathrm{g}}_\mu(s)} \Big/ \sum_{\nu=1}^{N_{\mathrm{vib}}} \frac{D_{n\mu}(s)^2}{k^{\mathrm{g}}_\nu(s)} \tag{7a}$$

$$k^a_n(s) = 1 \Big/ \sum_{\nu=1}^{N_{\mathrm{vib}}} \frac{D_{n\mu}(s)^2}{k^{\mathrm{g}}_\nu(s)} \tag{7b}$$

$$m^a_n(s) = 1/G_{nn}(s) \tag{7c}$$

$$\omega^a_n(s) = \sqrt{\frac{k^a_n(s)}{m^a_n(s)}} \tag{7d}$$

where $D_{n\mu}(s)$ is an element of the $\boldsymbol{D}$-matrix that connects normal coordinates with internal coordinates and $G_{nn}(s)$ is an element of the Wilson $\boldsymbol{G}$-matrix. Generalized adiabatic modes can be transformed from normal mode space into Cartesian coordinate space according to eqn. (8)

$$(\boldsymbol{a}^{\mathrm{g}}_n(s))_i = \sum_{\mu}^{N_{\mathrm{vib}}} (\boldsymbol{l}^{\mathrm{g}}_\mu(s))_i (\boldsymbol{a}^{\mathrm{g}}_n(s))_\mu \tag{8}$$

for $i = 1, \ldots, 3K$ where $(\boldsymbol{l}^{\mathrm{g}}_\mu)_i$ is component i of normal mode vector $\boldsymbol{l}^{\mathrm{g}}_\mu$ expressed in Cartesian coordinates.

2.2 Curvature vector and generalized normal modes expressed in terms of generalized adiabatic modes

Normal modes and curvature vector can be analyzed utilizing the amplitude $A_{n,s}(s)$.[1,5]

$$A_{n,s}(s) = \frac{\boldsymbol{k}(s)^\dagger \boldsymbol{M}(s) \boldsymbol{a}^{\mathrm{g}}_n(s)}{[(\boldsymbol{a}^{\mathrm{g}}_n(s))^\dagger \boldsymbol{M}(s) \boldsymbol{a}^{\mathrm{g}}_n(s)]^{1/2}} \tag{9}$$

which characterizes the curvature vector $\boldsymbol{k}(s)$ in terms of generalized adiabatic modes associated with internal parameters used to describe the reaction system. According to eqn. (9), curvature coupling coefficients $A_{n,s}$ possess the same dimension as coefficients $B_{\mu,s}$ and become identical to the latter for $\boldsymbol{l}^{\mathrm{g}}_\mu = \boldsymbol{a}^{\mathrm{g}}_n$. Both curvature vector and normal modes orthogonal to the reaction path are characterized within URVA in terms of generalized adiabatic internal modes.[1,2]

2.3 Analysis of the reaction path vector

The vector $\boldsymbol{t}(s)$ is decomposed into basis vectors $\boldsymbol{u}_n(s)$

$$\boldsymbol{u}_n(s) = \boldsymbol{M}^{-1} \boldsymbol{b}_n(s) \tag{10}$$

$$\boldsymbol{t}(s) = \sum_{n=1}^{3K-L} t_n(s) \boldsymbol{u}_n(s) \tag{11}$$

where an element i of $\boldsymbol{b}_n(s)$ is given by $\partial q_n(x)/\partial x_i$ and coefficients $t_n(s)$ were determined in ref. 1. Vectors $\boldsymbol{u}_n$ in eqns. (10) and (11), which were first suggested by Kato and Morokuma,[11] are the internal modes that characterize the movement along the reaction path and, therefore, they represent the equivalent to the AIMs used in the analysis of the transverse normal mode vibrations.[1] Generalizing the definition of a parameter set independent amplitude[1,5] for the case of the

reaction path vector, amplitude $A_{n,s}(t, s)$ is defined:

$$A_{n,s}(t, s) = \frac{(\boldsymbol{g}^{\dagger}\boldsymbol{M}^{-1}\boldsymbol{b}_n)^2}{(\boldsymbol{g}^{\dagger}\boldsymbol{M}^{-1}\boldsymbol{g})(\boldsymbol{b}_n^{\dagger}\boldsymbol{M}^{-1}\boldsymbol{b}_n)} \quad (12)$$

which considers (besides electronic effects) the kinetic aspect of the translational motion along the reaction path. Alternatively, one can use as a metric the unit matrix $\boldsymbol{I}$ and, by this, consider just electronic effects, which influence the direction of the reaction path:

$$A^{el}_{n,s}(t, s) = \frac{(\boldsymbol{g}^{\dagger}\boldsymbol{b}_n)^2}{(\boldsymbol{g}^{\dagger}\boldsymbol{g})(\boldsymbol{b}_n^{\dagger}\boldsymbol{b}_n)} \quad (13)$$

Both definitions (12) and (13) can be used in the analysis of $\boldsymbol{t}(s)$ although amplitude (12) should be given preference.

2.4 Quantum chemical methods

Four different levels of theory, ranging from HF to second order Møller–Plesset (MP2) perturbation theory,[42] density functional theory (DFT),[43] and coupled cluster (CC) theory[44] with all single (S) and double (D) excitations and a perturbative inclusion of the triple (T) excitations (CCSD(T)[45]), were applied to investigate the stationary points along the path of reaction I. Three basis sets were used for this purpose, namely Pople's 6-31G(d,p) basis set (basis A),[46] the augmented VTZ + P basis 6-311++G(3df,3pd) (basis B),[47] and for the CCSD(T) calculations Dunning's cc-pVTZ basis (basis C).[48] In the case of the DFT calculations, Becke's hybrid functional B3LYP[49] was applied because this was also used in related studies and despite the notorious underestimation of TS energies[50] provides a reliable account of the energetics of chemical reactions. Vibrational frequencies were calculated at the MP2 and B3LYP levels of theory with both basis A and B to determine the nature of the stationary points of reaction I and to calculate thermochemical data. In addition, the relative enthalpies $\Delta H(298)$ of complex **3** and product **5** were checked by carrying out G2 calculations.[51] Reliable calculations of **3** and the reaction energy of I require a correction of the basis set superposition error (BSSE).[52] In the case of **3**, we used the counterpoise method[53] to assess the stability of the van der Waals complex. This approach, however, is no longer reliable when calculating the reaction energy, which, if determined directly from the energies (enthalpies) of **1**, **2** and **5**, suffers from the fact that a one- and a two-heavy atom system is compared with a three-heavy atom system where the latter benefits from the full number of basis functions used for the RC while the former two are described by just subsets of this number. Hence, **5** is better described than **1** or **2**, which leads to an exaggeration of the exothermicity of reaction I. We eliminated the BSSE by comparing I with reaction II

$$HC{\equiv}CH + FH \rightarrow H_2C{=}CHF \quad \text{(reaction II)}$$

The combination I–II leads to reaction III:

$$H_2C{=}CHF + H_2C{=}CH_2 \rightarrow HC{\equiv}CH + CH_3CH_2F \quad \text{(reaction III)}$$

Reaction enthalpy I is obtained without (or a strongly reduced) BSSE by subtracting from the calculated reaction enthalpy of III the experimental value of the reaction enthalpy for II because the calculated $\Delta_R H(III)$ suffers only from a small BSSE and the experimental $\Delta_R H(II)$[54] cannot have any BSSE.

2.5 Reaction complex and reaction path

The parameters describing the RC are given in Scheme 2. The RC following the reaction path possesses in the entrance channel of I C_{2v} symmetry; it changes at **3** to C_s symmetry, at TS **5b** to C_1 symmetry, and finally at **5a** back to C_s symmetry. In the calculations, C_s symmetry of the RC was imposed to describe the region between **3** and **5b** because formation of

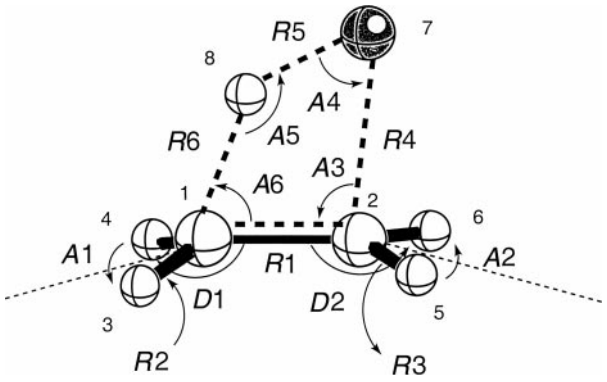

Scheme 2

complex **3** and rotation of **5** are low energy processes of little mechanistic relevance. Hence, the geometry of the RC is determined by 11 geometrical parameters, which were used throughout all calculations. For the purpose of the analysis in terms of AIMs, redundant internal coordinate sets were employed to facilitate the description. It is an advantage of the AIM concept that augmentation of the internal coordinate set does not change AIM contributions associated with individual coordinates.[1,2,5,6] After TS **4**, the reaction path passes a valley-ridge inflection (VRI) point where the reaction valley splits into two valleys. However, the VRI point is not a stationary point and, therefore, the IRC follows the ridge between the two valleys up to the next stationary point, which corresponds to the TS **5b** of internal rotation in **5** (Scheme 1). At TS **5b**, the RC adopts C_1-symmetry and the reaction path bifurcates according to clockwise or counter-clockwise rotation at the CC bond to the more stable staggered forms **5a**′ or **5a**. Also, the URVA algorithm makes it possible to follow the reaction path at a bifurcation point, we stopped the IRC calculation close to **5b** because the rotational process is not important for the reaction mechanism of I.

Preliminary URVA calculations were carried out at the HF/A and MP2/A level of theory using a constant step length of 0.05 $u^{1/2}\ a_0$. These calculations revealed that important features of the reaction path are qualitatively described already at the HF level. However, at a step length of 0.05 $u^{1/2}\ a_0$ neither HF nor MP2 calculations provide the basis for a detailed analysis of curvature coupling coefficients because avoided crossings between vibrational modes possessing the same symmetry are not correctly resolved. Therefore calculations were repeated at the B3LYP/A level of theory using a step size of 0.01 $u^{1/2}\ a_0$ in connection with the DMO procedure of Konkoli *et al.*,[55] by which all avoided crossings of the vibrational modes along the reaction path could correctly be resolved, and a reliable analysis of curvature coupling and mode–mode coupling coefficients was possible. In this way, the whole reaction range $-7.5 < s < 4\ u^{1/2}\ a_0$ reaching from complex **3** to product **5** was investigated (for comparison: Kato and Morokuma[11] could only investigate the range $-3 < s < 0.5\ u^{1/2}\ a_0$ because of computational limitations). For each value of the reaction coordinate s, the reaction path vector $\boldsymbol{t}(s)$ and its decomposition in terms of internal coordinate modes $\boldsymbol{u}_n$, the forces exerted on the atoms of the RC, the $3K-7$ generalized normal modes $\boldsymbol{l}^g_\mu(s)$ with associated frequencies $\omega^g_\mu(s)$, the decomposition of $\boldsymbol{l}^g_\mu(s)$ in terms of generalized adiabatic internal modes $\boldsymbol{a}^g_n(s)$, the adiabatic force constants k^a_n associated with the internal coordinates given in Scheme 1, reaction path curvature $\kappa(s)$, coupling coefficients $B_{\mu,s}$ and $B_{\mu,\nu}$, and the electron density distribution $\rho(\boldsymbol{r},s)$ were calculated.

2.6 Electron density analysis and analysis of forces

The forces exerted on the atoms of the RC along the reaction path are analyzed with the help of the electron density dis-

tribution $\rho(\boldsymbol{r},s)$. Changes in $\rho(\boldsymbol{r},s)$ reflect electronic structure changes, which can directly be related to properties of the PES along the reaction path as given by the negative gradient (forces on the atoms) and the Hessian matrix (force constants). The electron density distribution $\rho(\boldsymbol{r},s)$ determines all changes in the geometry of the RC along the reaction path, which are related to changes in the reaction path vector $\boldsymbol{t}(s)$ and the curvature vector $\boldsymbol{k}(s)$. The electron density distribution $\rho(\boldsymbol{r},s)$ of the RC was analyzed by generating along the path contour line diagrams of the difference density distribution $\Delta\rho(\boldsymbol{r},s)$ calculated according to

$$\Delta\rho(\boldsymbol{r},s) = \rho(\boldsymbol{r},s)[\text{reaction complex}] - \rho(\boldsymbol{r},s)[\text{procomplex}] \quad (14)$$

where the procomplex was defined by non-interacting **1** and **2** arranged in the geometry of the RC and BSSE corrected. In addition, the Laplace concentrations $-\nabla^2\rho(\boldsymbol{r},s)$ were investigated where, for both $\rho(\boldsymbol{r},s)$ and its associated Laplace concentration, MP2 response densities[56] were used. All calculations needed for URVA were carried out with the program ADIA, which is a multipurpose package for the analysis of vibrational spectra and carrying out of the URVA.[5,6] ADIA is a part of the *ab initio* package COLOGNE2000.[57] For the DFT and CCSD(T) calculations, the *ab initio* packages GAUSSIAN 98[58] and a local version of ACESII[59] were used.

3 Analysis of reaction path and reaction valley

Calculated energies and geometries of the stationary points investigated in this work are summarized in Tables 2 and 3. Details of the reaction path and the reaction valley are shown in Fig. 1 (energy profile $V(s)$), Fig. 2 (changes in the geometrical parameters $q(s)$ of the RC), Fig. 3 (internal coordinate contributions to reaction path vector $\boldsymbol{t}(s)$), Fig. 4 (internal forces

Table 2 Energetics of reaction I[a]

Method/ basis set	Energy E **1** + **2**[b]	Relative energy ΔE **3**	**4**	**5a**	**5b**	Enthalpy H **1** + **2**[b]	Relative enthalpy $\Delta H(298)$ **3**	**4**	**5a**	**5a**[c]	**5b**
HF/A	−178.051 80	−3.1	63.2	−21.1	3.6	−177.979 83	−1.9	60.2	−17.7	−10.6	3.1
MP2/A	−178.526 78	−3.2	51.0	−21.8	4.0	−178.457 53	−2.0	48.5	−18.0	−14.2	3.3
MP2/B	−178.803 08	−4.1	52.1	−14.8	3.4	−178.733 83	−2.9	49.6	−11.0	−14.1	2.7
B3LYP/A	−179.023 34	−4.0	43.2	−25.2	3.6	−178.955 61	−2.9	40.4	−21.9	−6.9	2.9
B3LYP/B	−179.109 24	−4.4	47.6	−16.1	3.0	−179.041 74	−3.2	44.8	−12.9	−8.9	2.5
G2	−178.765 94	−4.9		−16.6		−178.758 64	−3.7		−13.4	−11.7	
CCSD(T)/A	−178.571 24	−2.9	52.6	−20.5	3.6	−178.569 33	−1.6	49.8	−17.2	−10.0	3.1
CCSD(T)/C	−178.824 26	−3.5	53.3	−15.9	3.2	−178.756 76	−2.2	50.5	−12.6	−11.4	2.7
Exp.								48.1 ± 1.0		−10.3 ± 0.4	2.7 ± 0.4[d]

[a] Energies are given in hartrees, relative energies in kcal mol^{-1}. A corresponds to the 6-31G(d,p) basis set, B to 6-311++G(3df,3pd), and C to cc-pVTZ. Activation energies (enthalpies) are given relative to **3**, reaction energies (enthalpies) relative to **1** + **2**, and the energy of **5b** (rotational barriers between) relative to that of **5a**. For the calculation of CCSD(T)/A and CCSD(T)/C enthalpies, B3LYP/B frequencies were used. [b] All values BSSE corrected. [c] Corrected according to reaction III (see text). [d] Derived from the experimental ΔG value of 3.3 ± 0.4 kcal mol^{-1} [26] using calculated entropy values.

Table 3 Geometries of stationary points **1**–**5** calculated at B3LYP, MP2 and CCSD(T)[a]

	CH_2=CH_2 (**1**)							Complex **3**			
	*R*1	*A*1			FH (**2**) *R*5			*R*1	*R*5	*R*6	*A*1
B3LYP/A	1.330	116.4			0.925			1.335	2.258	0.933	116.5
B3LYP/B	1.325	116.5			0.922			1.329	2.259	0.933	116.6
MP2/A	1.334	116.9			0.921			1.338	2.302	0.926	117.0
MP2/B	1.329	117.3			0.916			1.333	2.221	0.926	117.5
CCSD(T)/A	1.340	116.6			0.921			1.343	2.342	0.925	116.8
CCSD(T)/C	1.333	117.2			0.916			1.336	2.253	0.923	117.3
TS **4**	*R*1	*R*4	*R*5	*R*6	*A*1	*A*2	*A*3	*A*4	*A*5	*D*1	*D*2
B3LYP/A	1.406	1.885	1.250	1.360	116.5	115.4	92.6	59.9	133.9	155.8	168.2
B3LYP/B	1.397	1.949	1.325	1.307	116.9	116.3	92.4	56.4	136.4	157.8	172.1
MP2/A	1.399	1.846	1.233	1.355	117.1	115.6	93.7	59.7	136.1	156.5	166.6
MP2/B	1.394	1.871	1.290	1.317	118 > .0	116.3	94.5	57.2	134.5	160.6	168.3
CCSD(T)/A	1.407	1.872	1.241	1.348	116.7	115.7	92.4	59.8	134.6	154.5	168.5
CCSD(T)/C	1.402	1.872	1.266	1.329	117.5	116.4	93.1	58.7	135.2	156.9	169.0
	CH_3CH_2F (**5a**)						CH_3CH_2F (**5b**)				
	*R*1	*R*4	*A*3				*R*1	*R*4	*A*3		
B3LYP/A	1.516	1.393	109.8				1.534	1.394	110.3		
B3LYP/B	1.510	1.399	110.1				1.526	1.401	110.3		
MP2/A	1.507	1.397	109.4				1.524	1.397	109.9		
MP2/B	1.502	1.389	109.6				1.519	1.390	110.2		
CCSD(T)/A	1.513	1.395	109.6				1.529	1.399	109.9		
CCSD(T)/C	1.406	1.384	110.1				1.523	1.388	110.1		

[a] Bond lengths *Rn* in Å and angles *An* and *Dn* in degrees. Basis A, B and C correspond to the 6-31G(d,p), the 6-311++G(3df,3pd) and the cc-pVTZ basis sets, respectively.

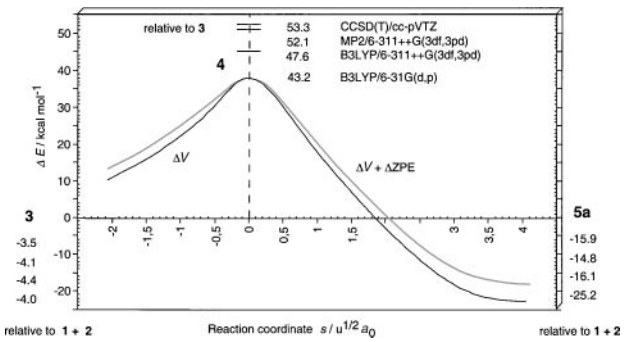

Fig. 1 B3LYP/6-31G(d,p) energies V (dark line) and $V + \mathrm{ZPE}$ (light line) as a function of the reaction path coordinate s for the reaction $FH + CH_2{=}CH_2 \rightarrow CH_3CH_2F$. The position of TS **4** corresponds to $s = 0\ u^{1/2}\ a_0$. For the barrier value, the energy of complex **3** (given on the left-hand side, BSSE corrected), for the reaction energy (given on the right-hand side) the energy of $FH + CH_2CH_2$ is taken as a reference. Results obtained at the MP2 and CCSD(T) level of theory are also given.

of the RC), Fig. 5 (difference electron density distributions $\Delta\rho(\boldsymbol{r},s)$), Figs. 6 and 7 (vibrational frequencies $\omega_\mu^g(s)$ and mode–mode couplings $B_{\mu,\nu}(s)$), Fig. 8 (decomposition of normal modes in terms of AIMs), Fig. 9 (adiabatic force constants), Figs. 10 and 11 (reaction path curvature and its decompositions into normal modes and AIMs). The analysis along the reaction path is based on Figs. 1–5, that of the $(3K - 7)$-dimensional orthogonal vibrational space on Figs. 6–11.

In the figures, in which a given property of the RC is represented as a function of s, the position of the TS is defined by a dashed vertical line at $s = 0$, *i.e.* the non-interacting reactants **1** and **2** are located at $s = -\infty$ and the product at $s = +\infty$ where the more interesting range $-2 < s < 4\ u^{1/2}\ a_0$ is given and the range of van der Waals complex **3** (-10 to -6), where changes are only moderate, is not shown.

3.1 Analysis of the one-dimensional reaction space

The analysis of the functions $V(s)$ and $q(s)$ ($q = \{Rn, An, Dn\}$, see Scheme 2) describing energy and geometry changes along the path $\tilde{\boldsymbol{x}}(s)$ are central to the study of the reaction mechanism. In addition, the investigation of the reaction path direction and the forces exerted on the atoms leads to important insights into the reaction mechanism when combined with the electron density analysis of the RC.

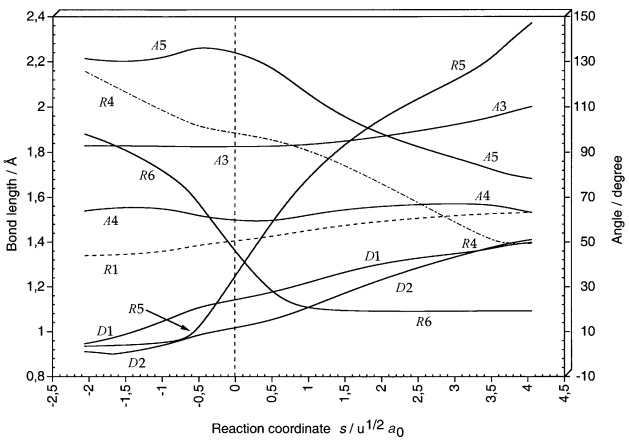

Fig. 2 B3LYP/6-31G(d,p) geometrical parameters q of the reaction complex RC given as a function of the reaction coordinate s. For a definition of parameters, compare with Scheme 2. The position of the TS corresponds to $s = 0\ u^{1/2}\ a_0$ and is indicated by the dashed vertical line.

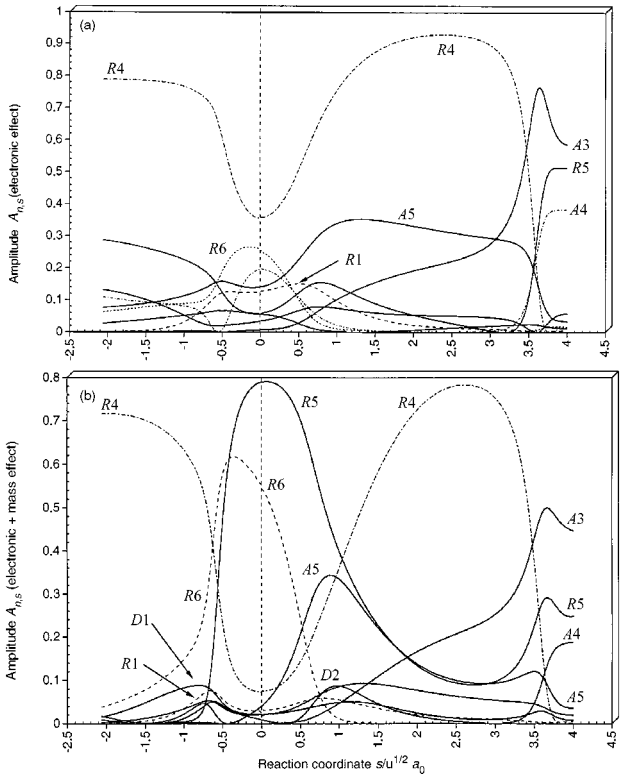

Fig. 3 Characterization of the reaction path vector $\boldsymbol{t}(s)$ in terms of internal coordinate modes using amplitudes $A_{n,s}$ considering (a) electronic and (b) electronic and mass effects according to eqn. (12). For a definition of parameters, compare with Scheme 2. The position of the TS corresponds to $s = 0\ u^{1/2}\ a_0$ and is indicated by the dashed vertical line. B3LYP/6-31G(d,p) calculations.

3.1.1 Energies and geometries at stationary points. Van der Waals complex **3** located in the entrance channel of reaction I is found to be 2–3 kcal mol^{-1} more stable ($\Delta H(298)$ values after BSSE corrections, Table 2) than **1** + **2**. Hence, the reaction barrier has to be measured relative to **3**, which was not always considered in previous work. The experimental activation enthalpy is 48.1 kcal mol^{-1} (Arrhenius activation energy: 49.3 kcal mol^{-1} (refs. 27, 28) which is well reproduced by both the MP2 (48.5 and 49.6 kcal mol^{-1}) and the CCSD(T) calculations (49.8 and 50.5 kcal mol^{-1}, Table 3) while HF exaggerates and DFT underestimates the activation enthalpy for reasons that have been discussed in the literature.[11,50] Note-

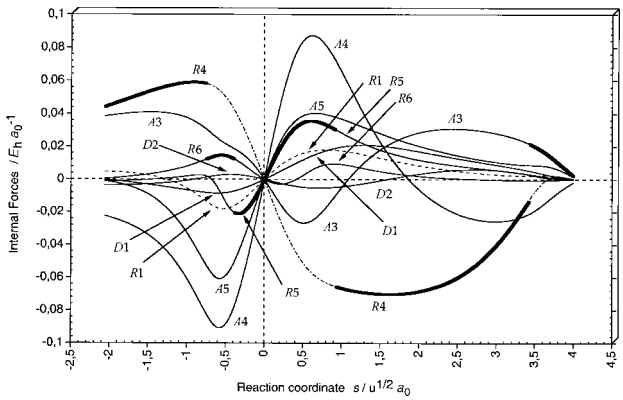

Fig. 4 Decomposition of the gradient in terms of attractive or repulsive internal forces. For a definition of internal coordinates *Rn*, *An* and *Dn*, compare with Scheme 2. The position of the TS corresponds to $s = 0\ u^{1/2}\ a_0$ and is indicated by the dashed vertical line. Internal forces associated with the internal coordinates that dominate the direction of the reaction path (compare with Fig. 3(b)) are given in bold.

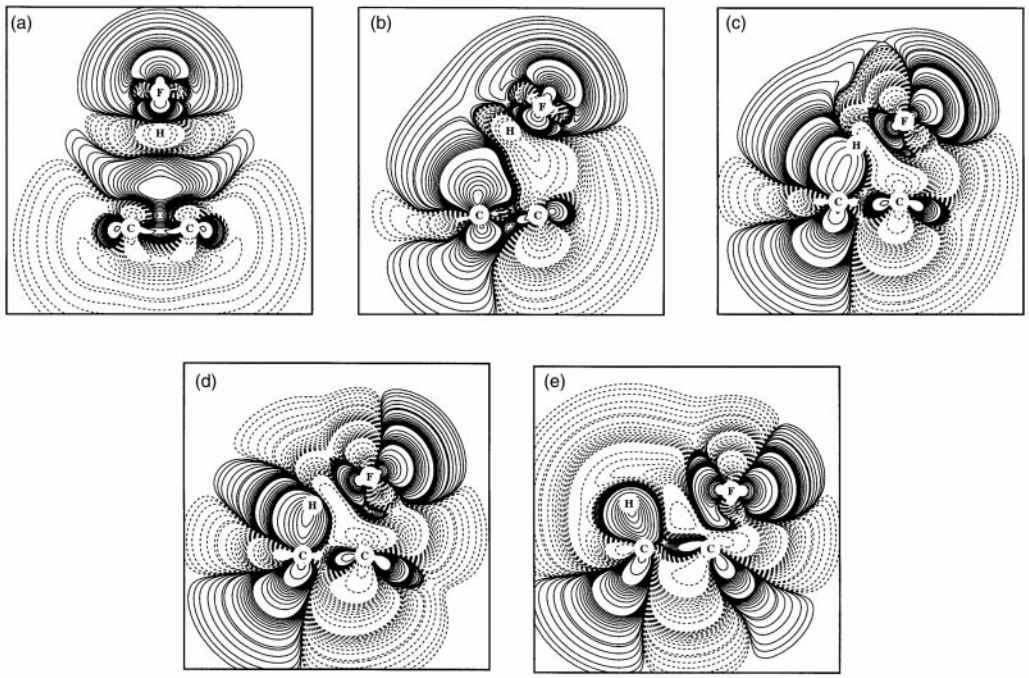

Fig. 5 Electron difference density distribution $\Delta\rho(\boldsymbol{r}, s)$ obtained at (a) $s = -8.0$ (van der Waals complex **3**, (b) $s = -4.2$, (c) $s = 0$ (TS **4**), (d) $s = 0.5$ and (e) $s = 3.8$ $u^{1/2}$ a_0. Solid contour lines indicate an increase, dashed contour lines a decrease, in the electron density relative to the electron density distribution of the procomplex (see text). MP2/6-31G(d,p) calculations.

worthy is that the experimental reaction enthalpy of -10.3 ± 0.4 kcal mol^{-1} at 298 K (calculated from exp. heats of formation: 12.45 (**1**), -64.8 (**2**) and -62.7 kcal mol^{-1} (**5a**)[54]) is poorly reproduced at most levels of theory where the better calculations settle in the range -11.0 (MP2/B) to -12.6 kcal mol^{-1} (CCSD(T)/C). We relate the difficulties in correctly calculating the reaction enthalpy to the difficulties in getting a balanced basis set description of one-, two- and three-heavy atom systems apart from the known problems of correctly describing F compounds.[60] BSSE corrections improve the reaction enthalpy by, maximally, 1.5 kcal mol^{-1}. Utilizing formal reactions II and III as described in Section 2, leads to a further improvement of 3 to 7 kcal mol^{-1} so that CCSD(T) and G2 values for $\Delta_R H(298)$ are -10.0, -11.4 and -11.7 kcal mol^{-1} (Table 2).

Since the reaction is investigated imposing C_s symmetry on the RC, the product **5** is forced to stay in the eclipsed conformation (**5b**). Rotation into the stable staggered conformation **5a** lowers the enthalpy by 2.7 kcal mol^{-1} (exp.: $\Delta G(298) = 3.3 \pm 0.1$ kcal mol^{-1}[26] corresponding to $\Delta H(298) = 2.7$ kcal mol^{-1} provided the calculated ΔS is used). Calculated geometries are listed in Table 3. Both CCSD(T) and B3LYP using a TZ + P basis (basis **B** or C) predict that **1** approaches **2** C_{2v}-symmetrically (T-shaped form) with the H of **1** sitting on the π-cloud of **2**. In this way both dispersion and induction interactions are maximized while exchange repulsion is kept low. The distance between H(**1**) to the midpoint of the CC bond of **2** is calculated to be 2.152 Å

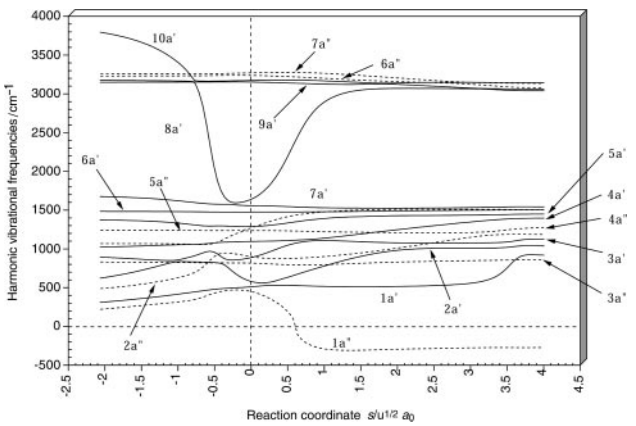

Fig. 6 DMO representation of normal mode frequencies $w_\mu(s)$, in which all avoided crossings are resolved. Symmetry symbols and numbering of normal modes are given according to the order of normal modes calculated at TS **4**. The position of the TS corresponds to $s = 0$ $u^{1/2}$ a_0 and is given by the dashed vertical line. The value $w_{1a''}(s) = 0$ indicates the location of the VRI point ($s = 0.6$ $u^{1/2}$ a_0). Imaginary 1a″ frequencies calculated for $s > 0.6$ $u^{1/2}$ a_0 are given as negative numbers. B3LYP/6-31G(d,p) calculations.

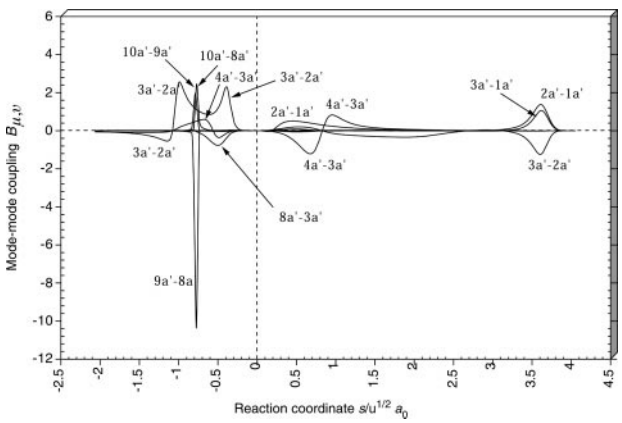

Fig. 7 Mode–mode coupling coefficients $B_{\mu,\nu}$ given as a function of s for a′-symmetrical modes of the RC of reaction I. All 45 mode combinations are considered and the $B_{\mu,\nu}(s)$ peaks are identified by appropriate mode labels. Large (absolute) $B_{\mu,\nu}(s)$ values mostly (but not exclusively; see 8a′-3a′) result from an avoided crossing where the shape of the $B_{\mu,\nu}(s)$ peak indicates either diabatic energy transition (sharp peaks such as 9a′-8a′) or energy dissipation between the modes (broad peaks). The position of the TS corresponds to $s = 0$ $u^{1/2}$ a_0 and is given by the dashed vertical line. B3LYP/6-31G(d,p) calculations.

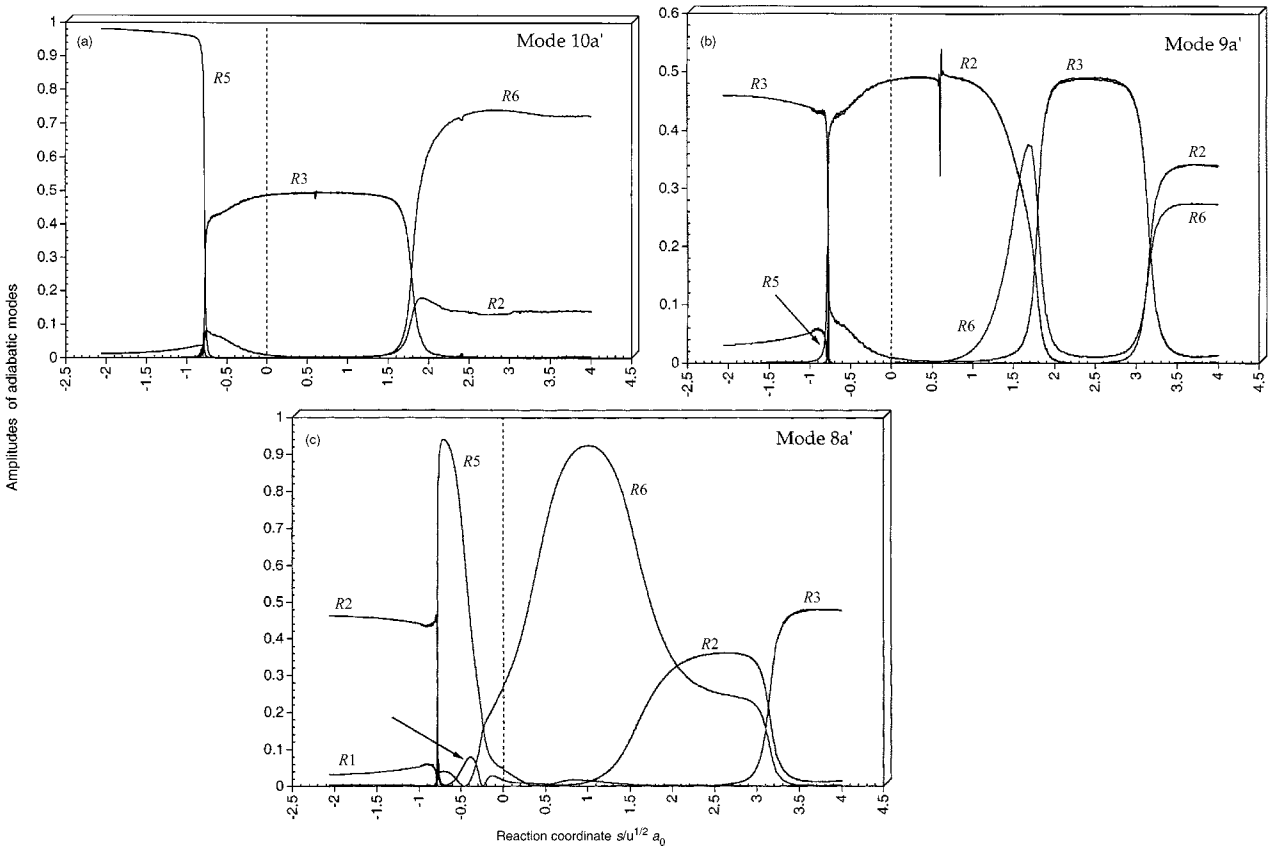

Fig. 8 Characterization of mode (a) 10a′ (b) 9a′, and (c) 8a′ in terms of generalized AIMs. For a definition of parameters, compare with Scheme 2. The position of the transition state corresponds to $s = 0$ u$^{-1/2}$ a_0 and is indicated by a dashed vertical line. B3LYP/6-31G(d,p) calculations.

(CCSD(T)/cc-pVTZ) corresponding to a H, C distance of 2.25 Å. The FH bond is lengthened from 0.916 to 0.923 Å, which suggests some small charge transfer from the π-orbital of **2** into the σ*(FH) orbital. The geometry of TS **4** varies considerably with method and basis set (Table 3). The approach parameters *R*6 and *R*4 (see Scheme 2) are 1.329 (MP2: 1.317; B3LYP: 1.307, Table 3) and 1.872 (MP2: 1.871; B3LYP: 1.949), respectively, at the CCSD(T)/cc-pVTZ level of theory suggesting a highly asymmetrical TS with C1–H8 bonding preceding C2–F7 bonding. B3LYP exaggerates bonding interactions between C1 and H8 thus leading to increased H8–F7 bond cleavage at TS **4**, which is reflected by the calculated bond lengths (B3LYP: 1.325; MP2: 1.290; CCSD(T): 1.266 Å, Table 3) and the low DFT barrier.

3.1.2 Changes in the geometry of the reaction complex. As Fig. 2 reveals, strong changes in bond lengths and interaction distances *R*4 and *R*6 occur at three different points along the reaction path, namely at -1.0 to -0.5, at 0.5 to 1.0 and at 3.6 u$^{1/2}$ a_0. These changes indicate strong changes in the electronic structure of the RC, which can be related features of the reaction path vector and to the curvature vector (see below).

3.1.3 Reaction path direction. Fig. 3 gives the internal coordinate contributions projected out of the reaction path vector. Parameter *R*4 dominates the direction of the reaction path vector $\boldsymbol{t}(s)$ apart from the region close to the TS and the region beyond $s = 3.5$ u$^{1/2}$ a_0 (Fig. 3(b); kinetic analysis according to eqn. (12), *i.e.* consideration of both electronic and mass effects). Close to the TS there are significant contribu-

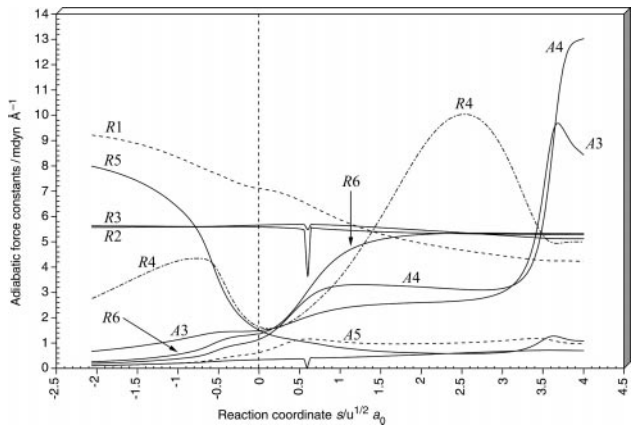

Fig. 9 Generalized adiabatic force constants associated with the internal parameters described in Scheme 2. The position of the TS corresponds to $s = 0$ u$^{1/2}$ a_0 and is indicated by the dashed vertical line. The wiggles at $s = 0.6$ u$^{1/2}$ a_0 indicate the position of the bifurcation point. B3LYP/6-31G(d,p) calculations.

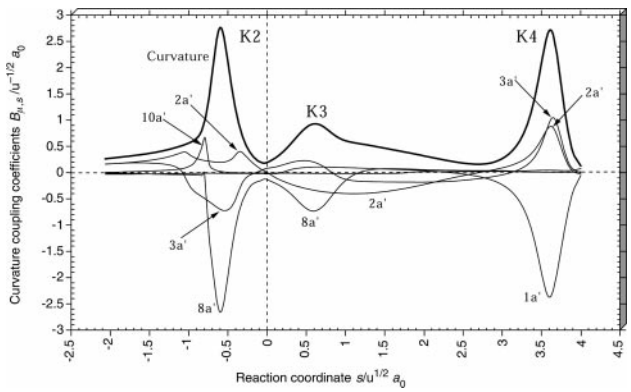

Fig. 10 Decomposition of the scalar reaction path curvature $\kappa(s)$ (thick solid line) in terms of normal mode-curvature coupling coefficients $B_{\mu,s}(s)$ (thin lines) where each mode μ is indicated. Curvature peaks are numbered K2, K3 and K4. The position of the TS corresponds to $s = 0$ u$^{1/2}$ a_0 and is indicated by the dashed vertical line. B3LYP/6-31G(d,p) calculations.

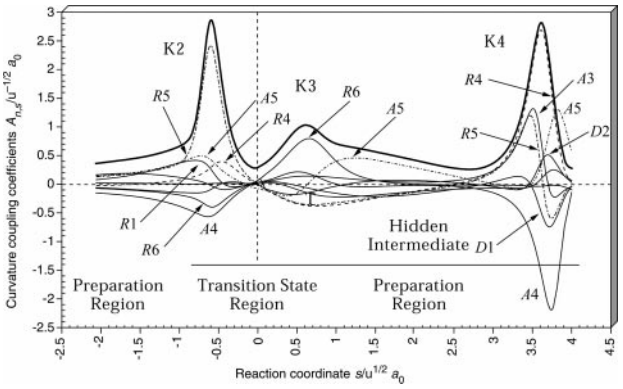

Fig. 11 Decomposition of the scalar reaction path curvature $\kappa(s)$ (thick solid line) in terms of adiabatic mode-curvature coupling amplitudes $A_{n,s}(s)$ (thin and dashed lines). The curve $\kappa(s)$ is shifted by 0.1 unit to more positive values to facilitate the distinction between $\kappa(s)$ and $A_{n,s}(s)$. A redundant coordinate set was used for the analysis (see text). Curvature peaks and reaction regions are indicated. For a definition of parameters, compare with Scheme 2. The position of the TS corresponds to $s = 0$ $u^{1/2}$ a_0 and is indicated by the dashed vertical line. B3LYP/6-31G(d,p) calculations.

tions from parameters *R*6, *R*5, and even *R*1 (Fig. 3). Beyond 3.5 $u^{1/2}$ a_0 the FCC angle (*A*3) and *R*5 become important. In the entrance channel, *R*4 plays the role of an approach distance, which determines largely the direction of the reaction path. At the TS, *R*5 and *R*6 take over this role because they are the internal coordinates of the FH bond (bond to be broken) and the C1–H8 bond (bond to be formed). In the exit channel, *R*4 dominates again, but now as the internal coordinate of the CF bond, which is formed in this region. There seem to be two regions of chemical relevance, in which two separated chemical events take place: at the TS the FH bond cleaving and CH bond forming process (characterized by large values of the *R*5 and *R*6 components) and in the exit channel the CF bond formation as a separate chemical process. *A priori*, one could expect that CH and CF bond formation take place at the same time in the TS region; however, their separation (CH bond formation close to $s = 0$ and CF bond formation close to $s = 3.5$) seems to be in contradiction with the fact that I is a concerted (one-step) reaction without a chemical intermediate. In the following, this contradiction has to be resolved.

Internal forces. The forces exerted on the atoms of the RC are given in Fig. 4 in terms of internal (coordinate) forces, which are directly related to the internal coordinates used to describe the RC. For reaction coordinates $s = 0$, -8 $u^{1/2}$ a_0 (position of **3**), $-\infty$, and $-\infty$, *i.e.* at the stationary points along the reaction path all internal forces have to be zero. In all other regions along the reaction path, the internal forces adopt either positive values, indicating atom–atom repulsion, or negative values, indicating atom–atom attraction. In Fig. 4, the forces associated with those internal coordinates that dominate the reaction path direction are given in bold. In the entrance channel the energy increase is caused predominantly by a repulsive *R*4-force; shortly before the TS, first the *R*6- and then the *R*5-force take over up to $s = 0.9$ $u^{1/2}$ a_0; in the exit channel, the *R*4-force dominates as an attractive force. In each case, the stabilizing or destabilizing character of a particular force has to be derived considering that a repulsive (attractive) force in a bond breaking (forming) process drives the reaction forward and *vice versa*. Hence, the attractive *R*1, *R*5 forces in the entrance channel indicate the resistance of **1** or **2** to lengthen the FH or CC bond, respectively, thus slowing down the reaction. Inspection of the difference density distribution $\Delta\rho(\boldsymbol{r})$ at $s = -4.2$ $u^{1/2}$ a_0 (Fig. 5(b)) reveals that the repulsive *R*4-force in the entrance channel results from exchange repulsion between F and C2 (H and C1). Exchange repulsion leads to polarization of the FH bond pushing density from the H to the F atom. This is similar to the situation in **3** (Fig. 5(a)); however, because of the breaking of the C_{2v} symmetry of **3**, polarization of the electron density occurs also along the CC bond in the way that π density is pushed from C2 to C1 (Fig. 5(b)). Charge polarization leads to attractive interactions between **1** and **2**, which partially compensate exchange repulsion and the energy increase due to FH and CC bond lengthening. At the TS (Fig. 5(c)), atom H8 enters the region of positive π difference density accumulated at C1; force *R*5 becomes repulsive driving H8 and F7 apart. A strong attractive force *R*4 develops between C2 and F7, which is now the driving force of the reaction for the major part of the exit channel. The density at F7 orients in the direction of the π-hole at C2, pushing at the same time π-density at C1 to the back thus carrying H8 with it (Fig. 5(d)). At $s = 3.8$ $u^{1/2}$ a_0, the positive difference density is close to linking C2 and F7 (Fig. 5(e)). In the last stage ($s > 3.8$), the force associated with *A*3 (repulsive for $s > 1$) causes a widening of the FCC angle and the adoption of the final structure of **5b**. Noteworthy is that shortly after the TS a situation is encountered (Fig. 5(d)), in which the F atom is neither bonded to H8 (because H8 is now bonded to C1) nor to C2. Since F is partially negatively charged and H_3CCH_2 partially positively charged in this situation, one can speak of a transient intermediate with partial ion pair character existing in the region $1 < s < 3$ $u^{1/2}$ a_0.

3.2 Analysis of the reaction valley

Investigation of the $3K - 7$-dimensional vibrational space is important for an understanding of the reaction mechanism, in particular for a description of energy transfer and energy dissipation. Electronic changes as reflected by the changes in the density distribution (Fig. 5) and their subsequent changes in the energy (Fig. 1) are reflected by geometrical changes of the RC (Fig. 2), the forces exerted on the atoms of the RC (Fig. 4), the reaction path direction (Fig. 3), and the reaction path curvature (Fig. 10). The latter indicates a possible coupling of the translational mode along the reaction path and the vibrational modes (for $\omega_\mu(s)$, see Fig. 6). Another link between electronic changes and features of the reaction path is provided by the analysis of the adiabatic force constants (Fig. 9), which provide information on electronic changes, vibrational mode features, and properties of the reaction path.

3.2.1 Normal mode frequencies. The RC of reaction I possesses 17 vibrational modes, 10 of a′ symmetry and 7 of a″ symmetry. Molecules **1** and **2** have together 13 vibrational modes while product **5b** has 18 vibrational modes, *i.e.* of the 11 translational and rotational degrees of freedom of the reactants four are converted into vibrational modes and one into the translational mode along the reaction path. In Fig. 6, the vibrational frequencies $\omega_\mu^g(s)$ of the RC are shown. The frequency diagram reveals that the VRI point is encountered at $s = 0.6$ $u^{1/2}$ a_0 where the frequency of mode 1a″, which corresponds to a CH_2 twisting mode (partial rotation at the CC bond axis), becomes imaginary (indicated in Fig. 6 by a frequency value <0). However, the VRI point is of no relevance for the IRC path (relevant for trajectory calculations because of the effective broadening of the valley) and, therefore, will not be considered further. Of particular interest are the a′ modes because they can couple with the C_s symmetrical motion of the RC along the reaction path. In the range $-2 < s < 4$ $u^{1/2}$ a_0, there are 12 avoided crossings between vibrational states (all with $v = 0$) involving a′-modes and these are indicated by the maxima and minima of the $B_{\mu,\nu}(s)$ diagram of Fig. 7. Strongly localized avoided crossings as represented by a close approach of the curves $\omega_\mu(s)$ lead to sharp peaks of $B_{\mu\nu}(s)$ while more delocalized mode–mode interactions, which imply that two vibrational states of the same

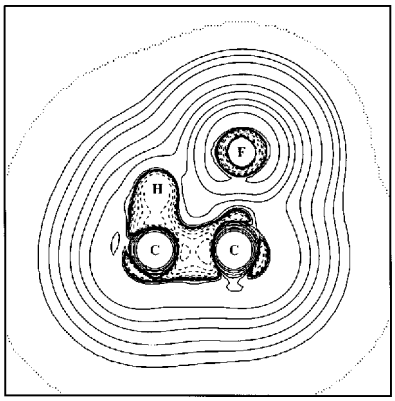

Fig. 12 Laplace concentration $-\nabla^2\rho(\boldsymbol{r}, s)$ obtained, calculated in the region of the hidden intermediate. Solid contour lines indicate depletion, and dashed contour lines show the concentration of the electron density distribution. MP2/6-31G(d,p) calculations.

symmetry accompany each other for a part of s, are represented by broader $B_{\mu\nu}(s)$ peaks (Fig. 7). At the positions of the sharp $B_{\mu\nu}(s)$ peaks *localized diabatic transitions* between two adiabatic modes take place so that both the character and the energy carried by the first mode is transferred to the second mode. Delocalized avoided crossings (broad curvature peaks) are characterized by a distribution of the energy carried by one mode over both modes so that energy dissipation can take place. In this way, the peaks of the mode–mode coupling coefficients $B_{\mu\nu}(s)$ shown in Fig. 7 provide direct information about energy transfer and the degree of energy dissipation between the vibrational modes. The pattern of the frequency diagram of Fig. 6 is reminiscent of the reaction $CH_3 + H_2 \rightarrow CH_4 + H$ and related substitution reactions previously investigated.[1,2] There is one mode, namely the FH stretching mode 10a′ (for $s < -0.8$ u$^{1/2}$ a_0), that changes strongly in the TS region by dropping from about 3900 to almost 1600 cm^{-1} and then raising again to 3100 cm^{-1} in the exit channel. Due to avoided crossing involving modes 9a′ and 8a′ (Figs. 6 and 7) the character of this mode changes as is demonstrated by its decomposition in terms of AIMs shown in Fig. 8. For example mode 10a′ changes at $s = 0.8$ u$^{1/2}$ a_0 from a FH stretching mode to become a CH stretching mode of CH spectator bonds ($R3$, Scheme 2). Another change at 1.8 u$^{1/2}$ a_0 (Fig. 8(a)) leads to CH stretching involving the newly formed CH bond ($R6$), which emerges from a point close to $s = 1.1$ u$^{1/2}$ a_0 (Fig. 8) and by this suggests the region where the new CH bond seems to be first established. However, inspection of the adiabatic mode decomposition of 9a′ and 8a′ (Figs. 8(b) and 8(c)) clarifies that the CH bond formation starts much earlier, namely at $s = -0.5$ u$^{1/2}$ a_0 (first $R6$ contribution in 8a′) and that $s = 1.1$ u$^{1/2}$ a_0 identifies the point, at which the CH bond formation is largely finished. This is also confirmed by the diagram of the adiabatic force constants $k_n^a(s)$ (Fig. 9): The $R6$ value adopts the magnitude of a normal CH force constant at $s = 1.1$ u$^{1/2}$ a_0. Major changes in $\omega_\mu(s)$ all occur in the TS region (Fig. 6). There is only a stronger change of mode 1a′ (describing FCC bending), which changes also significantly at $s = 3.5$ u$^{1/2}$ a_0. We note that the five lowest modes of complex **3** correspond to translations (3) and rotations (2) of separated **1** and **2**. At TS **4**, these modes are 1a″, 1a′, 2a′, 5a″ and 8a′ where the latter two have obtained this role by repeated avoided crossings along the reaction path. Fig. 7 (see also Figs. 6 and 8) reveals that energy stored in mode 10a′ (FH stretching mode in the entrance channel) is transferred by two diabatic transitions to mode 9a′ and then to mode 8a′, which before the TS becomes the FH stretching mode of the breaking FH bond as confirmed by the fact that frequency $\omega_{8a'}(s)$ decreases to 1600 cm^{-1} in the TS region (Fig. 6). If mode 8a′ couples with the motion along the reaction path mode, selective rate enhancement by laser pumping is possible as is discussed in the next subsection.

3.2.2 Reaction path curvature. The reaction path curvature $\kappa(s)$ (Fig. 10) of reaction I is characterized by four curvature peaks K1, K2, K3 and K4. The curvature peak K1 (not shown in Fig. 10) corresponds to the formation of van der Waals complex **3** in the range -10 to -6 u$^{1/2}$ a_0. We note that such a curvature peak was also found for reactions that do not proceed *via* a van der Waals complex[1,2] and, hence, a curvature peak early in the entrance channel is indicative of important van der Waals interactions irrespective whether these lead to a local minimum on the PES or not. Curvature peaks K2 and K3 are located at $s = -0.6$ and 0.6 u$^{1/2}$ a_0, *i.e.* close to the TS. They are associated with normal mode 8a′ and (to a smaller extent) with modes 10a′, 3a′ and 2a′ as the decomposition of $\kappa(s)$ in terms of normal mode contributions reveals (Fig. 10). If energy is stored in mode 10a′, it will be stepwise channelled with little energy dissipation into the reaction path mode thus enhancing the reaction rate. This prediction cannot be made if the mode–mode couplings are not known (Fig. 7). For the reverse reaction, energy should be pumped into mode 1a′, which encounters strong coupling with the reaction path motion at K4 (Fig. 10). This energy is dissipated into modes 2a′ and 3a′ as is obvious from the mode–mode couplings (Fig. 7), but since the latter also couple with the path motion, mode selective rate enhancement should also be possible for the reverse reaction. Curvature peak K4 located at 3.65 u$^{1/2}$ a_0 is clearly separated from K2 and K3; it is associated with modes 1a′, 2a′ and 3a′, which correspond to the CCF bending and the CF stretching motion. Again, this suggests two separated chemical processes, namely one close to the TS involving changes in FH/HC bonding and one in the exit channel involving changes in FC bonding. The decomposition of the scalar curvature in terms of adiabatic curvature couplings (Fig. 11) confirms that curvature peaks K2 and K3 are associated with internal coordinate modes $R5$ and $R6$, *i.e.* FH and CH bond stretching where the two change their roles from K2 to K3. Coefficient $A_{R5,s}$ is positive and dominant for K2, indicating that the polarization of the FH bond up to $s = -1$ u$^{1/2}$ a_0 and the concomitant polarization of **2** as documented by the difference density (Fig. 5) drives the F and the H atom apart, but C1–H8 interactions are still repulsive as reflected by the corresponding force (Fig. 4) and the negative coefficient $A_{R6,s}$ in this region. Clearly, FH bond breaking and CH bond formation occur simultaneously and the two curvature peaks K2 and K3 are associated with just one chemical process (transfer of H8 from F7 to C1). The crossing point of the $R5$ and $R6$ coefficients ($s = 0$ u$^{1/2}$ a_0, Fig. 11) denotes that reaction path point, at which the FH bond is half broken and the C1–H8 bond half formed. It happens to coincide with the location of the energetical TS. In recent work,[1,2] we have called the region between van der Waals peak K1 and the TS region defined by curvature peaks K2 and K3 as the *reactant preparation region*, in which the reaction partners prepare for the chemical reaction. In the case of reaction I, the preparation region is characterized by a long shoulder of K2 reaching from $s = -5.6$ to -1 u$^{1/2}$ a_0. In this region, the C=C bond is lengthened and polarized (contribution $R1$, Fig. 11) and molecule **1** rotates from the T-shaped into a side-on position (contributions $A4$ and $A5$), which is a slow process. A second preparation region seems to be indicated by the curvature shoulder between $K3$ and $K4$ ($1.0 < s < 3$ u$^{1/2}$ a_0), which is associated with the positioning of the F atom (contributions $R4$ and $A5$). The decomposition of $\boldsymbol{t}(s)$ (Fig. 3) reveals that in this region coordinate $R4$ becomes dominant and that there is a strong attraction between F7 and C2. Electron density analysis and natural bond orbital (NBO) analysis suggest that F7 and C2 carry in this region charges of -0.4 and $+0.4$, indicating that one can speak of partial ion pair character

between the ethyl cation and fluoride anion. This interpretation is supported by an analysis of the Laplace concentration $-\nabla^2_\rho(\boldsymbol{r},s)$ (Fig. 12), which shows an F atom neither bonded to H8 or C2 and an electron density concentration pattern reminiscent of an ion pair. This partial ion pair can be considered as a *hidden intermediate* because it does not correspond to an intermediate minimum on the PES, but plays a similar role to a real intermediate as we will show in Section 4. Thus, in the second preparation region (region between K2 and K3) the ion pair prepares for the forming of the CF bond of **5b**.

Curvature peak K4 defines the region in which the CF bond is formed ($3 < s < 4$ u$^{1/2}$ a_0). The strongest contributions to K4 are from *R*4 (CF stretch vibration, amplitude $A_{R4,\,s} > 0$: attraction between C2 and F, Fig. 11), *A*4, *A*3, *A*5, *R*5, *D*1 and *D*2 where the latter components all describe the adjustment of CF and CH bonds in **5b**. The adiabatic force constant associated with *R*4 reaches its maximum value at 4 u$^{1/2}$ a_0 (Fig. 9), indicating in this way that at this point the formation of the CF bond is finished.

4 Discussion of the reaction mechanism and chemical relevance of results

The curvature peaks suggest seven distinct regions along the path of reaction I: (1) Reactant region ($-\infty < s < -10$ u$^{1/2}$ a_0); very weak interactions between reactants without any chemical relevance; the reactants possess electronic structures that basically correspond to those of isolated molecules at their equilibrium geometries. (2) Van der Waals region ($-10 < -6$ u$^{1/2}$ a_0; region of curvature peak K1). Dispersion and induction interactions lead to the formation of van der Waals complex **3**. (3) Preparation region (between curvature peaks K1 and K2; Fig. 11). The reactants prepare for the reaction by mutual polarization when approaching each other, *i.e.* both the FH and the CC bonds are polarized. (4) Transition state region (region of curvature peaks K2 and K3; Fig. 11). The FH bond is broken while simultaneously the CH bond is formed; hidden intermediate **6** (Scheme 1) is formed possessing ion pair character. (5) Preparation region (between curvature peaks K3 and K4; Fig. 11): **6** is prepared for the formation of a covalent bond between the positively charged C2 and the negatively charged F7 atom. (6) Formation of **5b** (region of curvature peak K4). The C–F bond is formed. (7) Product region ($4 < s < \infty$ u$^{1/2}$ a_0; after the bifurcation point). Relaxation of **5** in its most stable form **5a**. Steps (1) to (7) will be encountered for addition of H–X or X–X (X: halogen) to ethylene or, in general, other alkenes. The important chemical events of reaction I take place in steps 4 and 6 with an intermediate preparation region that we associate with hidden intermediate **6**, which will occupy a stationary point and, by this, become a true intermediate as soon as the reaction takes place in a solvent with a sufficiently high dielectric constant ε (Scheme 1). The latter represents a scaling factor that reduces the attraction between cation and anion. Also, solvation shells will form around the ethyl cation and fluoride anion that will separate the two ions. Such an ion pair possesses a finite life time, *i.e.* **6** can be observed in the reaction. The reaction mechanism corresponds in this case to a nonconcerted reaction with a lower barrier (solvent stabilized TS) and a different stereochemistry. The reaction mechanism investigated for the situation in the gas phase indicates how the reaction will change if the environment changes. This information can be unraveled if one explores the reaction valley as done in this work. In previous work, we identified the TS region as the region with the largest curvature peaks.[1,2] The latter indicate chemical processes such as bond breaking or bond formation. Their height should be related to the force constant of the bond being formed or broken, *i.e.* to the bond strength. Clearly a FH bond is stronger ($D_0 = 136$ kcal mol^{-1}) than a CH bond ($D_0 = 98$ kcal mol^{-1}).[61] However, a rapid cleavage (formation) caused by sudden electronic changes leads to a higher curvature peak than a slow continuous cleavage (formation) of the bond. Hence, the relationship between bond strength and curvature peak has to be considered for each case separately. According to the previous definition, the TS region would comprise the region of peaks K2, K3 and K4 with its center being located at 1.5 u$^{1/2}$ a_0. Relative to this position TS **4** is shifted by 1.5 u$^{1/2}$ a_0 into the entrance channel in line with the Hammond postulate, which predicts for an exothermic reaction an early TS. Alternatively, one could consider that reaction I consists of a two-step reaction, the first step of which leads in an almost thermoneutral reaction (energy-TS and center of the transition state region K2–K3 are identical) to a partial ion pair while the second step yields in a strongly exothermic (the energy TS **4** is shifted 3.6 u$^{1/2}$ a_0 relative to K4 into the entrance channel) ion reaction product **5**. Although TS **4** is energetically the most important point of the reaction, mechanistically it is not because it represents just one point in the range of the curvature peaks K2–K3 (Fig. 11) associated with FH bond breaking and CH bond forming. The fate of the reaction is decided in the region of the van der Waals complex **3** and that of the hidden intermediate **6** as we will show in the following. Reaction I can be considered as a prototype for addition/cycloaddition reactions (Scheme 3) such as the H-exchange reactions (1) and (3), the hydrogenation reactions (2) and (4), the multiple bond addition reactions (5) and (6) or the cycloaddition reactions (7). Some of these reactions are just formal because they take, in reality, a different reaction path to avoid the high-energy TS of a symmetry-forbidden reaction. For example, the $H_2 + H_2$ reaction proceeds *via* a linear TS according to experimental results[38] and the reaction $HX + H_2$ leads to a T-shaped hypervalent XH_3 molecule rather than to H exchange.[62] However, in the sense that the reactions of Scheme 3 are model reactions for symmetry-forbidden pericyclic reactions they can be discussed on the basis of the reaction mechanism of I where one has to focus on the van der Waals complex possible for each reaction (Scheme 4), its conversion into a particular TS (Scheme 4), and the possibility of

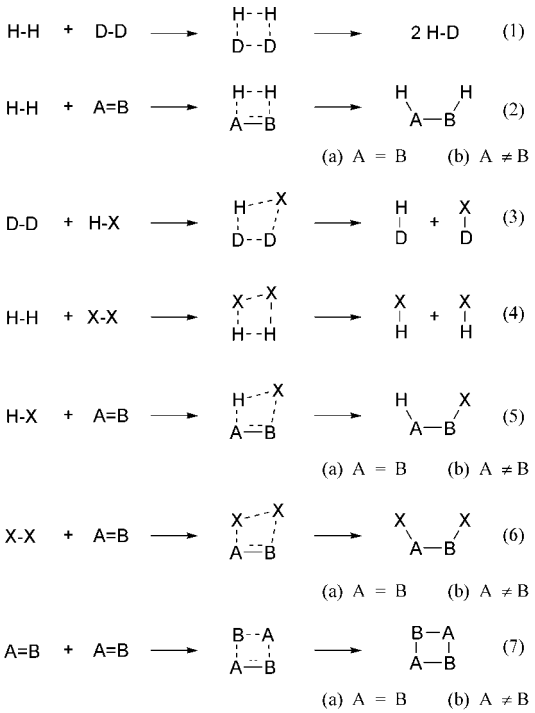

X : F, Cl, Br, I, NH_2, BH_2, OH, *etc.*

A=B : $H_2C{=}CH_2$, $HC{\equiv}CH$, $H_2C{=}O$; $H_2Si{=}CH_2$, *etc.*

Scheme 3

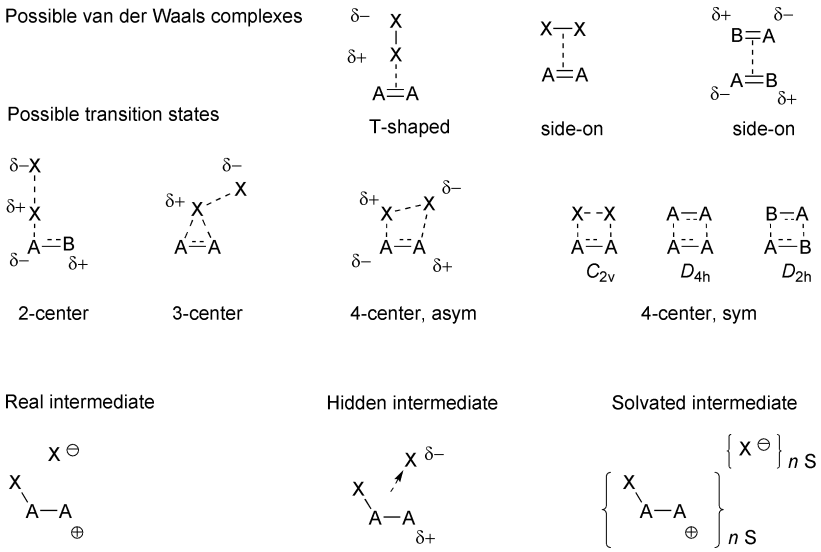

Scheme 4

a real or a hidden intermediate (Scheme 4). The mechanism of reaction I suggests that the structure of the TS is already determined at the stage of the van der Waals complex, which for reactions (1) to (7) could be either a T-shaped (or L-shaped for A ≠ B) complex, a side-on complex between nonpolar molecules or a side-on symmetric dipole–dipole complex. Clearly, the second choice is the least favorable because exchange repulsion interactions are large while stabilizing induction interactions remain small. Since the T-shaped complex is not stabilized for reactions (1) and (7) (for A = B: [2 + 2] cyloaddition of ethene, *etc.*), the latter will proceed (side on) *via* a high-energy TS typical of symmetry-forbidden reactions. The side-on approach is also found for polar A=B molecules because dipole–dipole attraction can compensate exchange repulsion (Scheme 4: possible van der Waals complexes). If the T-shaped complex can be formed, the complex stability will depend on the magnitude of existing multipole moments, the polarizability of the X–X bond (depending on the polarizability of X and related to the XX bond strength), the availability of a low-lying σ*(XX) orbital, and the possibility of charge transfer into this orbital from a high-lying π*(AA) orbital. Because of exchange repulsion the atom closest to the basis (A=A or other) will always be positively charged (H in HX, X in XX) and that farther away from the basis negatively charged (X in HX, Scheme 4). Accordingly, the T-shaped complex initiates an electrophilic rather than nucleophilic addition in the case of unsaturated hydrocarbons. Symmetry breaking due to an in-plane rotation will lead to a four-centered TS (Schemes 3, 4) in which the positively charged X atom (of XX) will always be closer to the A=A basis than the negatively charged X atom (asymmetrical TS, Scheme 4). This implies that the reaction splits up into two chemical processes as found for I: First, the X–X bond will be broken in a partially heterolytic fashion and the new A–X bond will be formed. In a second step, the formation of the other A–X will take place. Depending on how strongly the XX bond is polarized, a three-centered (strong polarization) or a four-centered TS (weaker polarization) is formed. The extremes of these two basically different situations can be found for the H exchange reaction (1) shown in Scheme 3, the uncatalyzed hydrogenation of ethene (2a) or the [2 + 2] cycloaddition of ethene on the one side and the Cl_2 or Br_2 addition to ethene (6) on the other side. The latter proceed *via* a three-centered TS[36] exhibiting a strongly polarized XX bond followed by the formation of a hidden intermediate $\{X–CH_2–CH_2^+, X^-\}$, which in solution converts into a real intermediate.[8,9,16] The more the four-centered TS adopts the character of a three-centered TS with a long C–X (A–X) distance the more pronounced is the hidden intermediate and, by this, the chance to convert it in another environment (solution) into a real intermediate. Since the nature of the TS depends on the electronic features of the van der Waals complex in the entrance channel, the complex indirectly determines the fate of the reaction after the TS. If the basis AB is strongly polar a two-centered TS becomes possible (*e.g.* HCl addition to silaethene[35]) and by this a more pronounced hidden intermediate (real intermediate in solution) is generated which in the gas phase, of course, is just a transient point on the PES representing the spontaneous combination of two oppositely charged species. We can relate the reaction mechanism to the number of curvature peaks. Two curvature peaks (of equal magnitude) will always occur in the case of symmetric fourcentered TSs such as for (1), (2) or (7) (Scheme 3). They represent the simultaneous breaking of old and forming of new bonds and, therefore, have to be considered (as in the case of reaction I) as one chemical event. Since a hidden intermediate can only occur between two different chemical events, a hidden intermediate is not possible in these cases. In the entrance channel, there will be a very small curvature peak corresponding to a weak van der Waals complex or just van der Waals interactions with little relevance for the reaction mechanism. Reaction (3) also possesses a highly symmetric TS (C_{2v} or equivalent) and, therefore, again four bonds will be changed in the TS in one chemical event thus leading to two curvature peaks symmetrically arranged relative to the energy TS. Again, there is no chance for a hidden intermediate and for a change of the reaction mechanism in a different environment (provided catalysis or specific solvation are excluded). The van der Waals complex could take two different forms, namely XH standing on the HH basis or HH standing on the FH basis where in the latter case multipole interactions lead to an L-shaped form (HH shifted to X = F or Cl), which turns out to be relevant for the reaction mechanism. It is known that the first complex leads to a lower energy reaction path.[62] Reactions (4), (5) and (6) proceed with three curvature peaks, representing two different chemical events between which a hidden intermediate can occur. The more pronounced the hidden intermediate is (reflected by the separation of the relevant curvature peaks, the charge distribution, the nature of the reaction path, *etc.*) the more likely is the chance that a change in the environment or the substitution pattern leads to a real intermediate. For example, alkyl groups which can stabilize the development of positive charge at one C in reaction I by hyperconjugation lead to a more pronounced hidden intermediate. All reactions considered in Scheme 3 are formally symmetry-forbidden reactions. However, the formation

of a T-shaped TS and the polarization of the bond to be broken will determine the asymmetry of the four-centered TS. The more asymmetric the latter becomes (leading finally to a three-centered or a two-centric TS) the more will electronic factors overrule symmetry considerations in line with the well-known fact that the Woodward–Hoffmann rules no longer apply to pericyclic reactions with strongly polar bonds.[7] A strongly asymmetric TS makes the existence of a hidden intermediate more likely. Inspection of the curvature peaks and adiabatic curvature coupling coefficients is the basis for reliable mechanistic predictions upon a change of the environment and the substituents.

Acknowledgement

This work was supported at Göteborg by the Swedish Natural Science Research Council (NFR). All calculations were done on the supercomputers of the Nationellt Superdatorcentrum (NSC), Linköping, Sweden. DC and EK thank the NSC for a generous allotment of computer time.

References

1 Z. Konkoli, E. Kraka and D. Cremer, *J. Phys. Chem. A*, 1997, **101**, 1742.
2 E. Kraka, in *Encyclopedia of Computational Chemistry*, ed. P. v. R. Schleyer, N. L. Allinger, T. Clark, J. Gasteiger, P. A. Kollman, H. F. Schaefer III and P. R. Schreiner, Wiley, Chichester, 1998, vol. 4, p. 2437.
3 W. H. Miller, N. C. Handy and J. E. Adams, *J. Chem. Phys.*, 1980, **72**, 99.
4 (*a*) K. Fukui, *J. Phys. Chem.*, 1970, **74**, 4161; (*b*) K. Fukui, *Acc. Chem. Res.*, 1981, **14**, 363.
5 (*a*) Z. Konkoli and D. Cremer, *Int. J. Quantum. Chem.*, 1998, **67**, 1; (*b*) Z. Konkoli, L. A. Larsson and D. Cremer, *Int. J. Quantum. Chem.*, 1998, **67**, 11; (*c*) Z. Konkoli, L. A. Larsson and D. Cremer, *Int. J. Quantum. Chem.*, 1998, **67**, 29.
6 D. Cremer, L. A. Larsson and E. Kraka, in *Theoretical and Computational Chemistry*, *Theoretical Organic Chemistry*, ed. C. Párkányi, Elsevier, Amsterdam, 1998, vol. 5, p. 259.
7 See, *e.g.*, R. B. Woodward and R. Hoffmann, *Angew. Chem. Int. Ed. Engl.*, 1969, **8**, 781.
8 T. H. Lowry and K. Schueller Richardson, *Mechanism and Theory in Organic Chemistry*, 3rd edn., Harper and Row, New York, 1987.
9 J. March, *Advanced Organic Chemistry*, *Reactions*, *Mechanisms and Structure*, 3rd edn., Wiley, New York, 1985.
10 *The Chemistry of Functional Groups*, *The Chemistry of Double-Bonded Functional Groups*, ed. S. Patai, Wiley, New York, 1972, vol. 2.
11 (*a*) S. Kato and K. Morokuma, *J. Chem. Phys.*, 1980, **73**, 3900; see also (*b*) S. Kato and K. Morokuma, *J. Chem. Phys.*, 1980, **72**, 206.
12 J. Del Bene, *Chem. Phys. Lett.*, 1974, **24**, 203.
13 D. Volkmann, B. Zurawski and D. Heidrich, *Int. J. Quantum. Chem.*, 1982, **22**, 631.
14 A. Hinchliffe, *Chem. Phys. Lett.*, 1982, **85**, 531.
15 J. A. Pople, J. Frisch and J. E. Del Bene, *Chem. Phys. Lett.*, 1982, **91**, 185.
16 A. M. Sapse and D. C. Jain, *J. Phys. Chem.*, 1984, **88**, 4970.
17 T. H. Tang, W. J. Hu, D. Y. Yan and Y. P. Cui, *J. Mol. Struct., THEOCHEM*, 1990, **207**, 319.
18 R. M. Minyaev and D. J. Wales, *Chem. Phys. Lett.*, 1994, **218**, 413.
19 Y. Kumeda and T. Taketsugu, *J. Chem. Phys.*, 2000, **113**, 477.
20 J. A. Shea and W. H. Flygare, *J. Chem. Phys.*, 1982, **76**, 4857.
21 (*a*) A. J. Barnes, H. E. Hallam and G. F. Scrimshaw, *Trans. Faraday Soc.*, 1969, **65**, 3172; (*b*) A. J. Barnes, J. B. Davies, H. E. Hallam and J. D. R. Howells, *J. Chem. Soc., Faraday Trans II*, 1973, **69**, 246.
22 S. A. McDonald, G. L. Johnson, B. W. Keelan and L. Andrews, *J. Am. Chem. Soc.*, 1980, **102**, 2892.
23 W. G. Read and W. H. Flygare, *J. Chem. Phys.*, 1982, **76**, 2238.
24 G. A. Olah, J. M. Bollinger and J. Brinich, *J. Am. Chem. Soc.*, 1968, **90**, 2587.
25 P. Kollman, J. McKelvey, A. Johansson and S. Rothenberg, *J. Am. Chem. Soc.*, 1975, **97**, 955.
26 P. H. Verdier and E. B. Wilson, Jr., *J. Chem. Phys.*, 1958, **29**, 340.
27 P. Cadman, M. Day and A. F. Trotman-Dickenson, *J. Chem. Soc. A*, 1970, 2498.
28 P. Cadman, M. Day and A. F. Trotman-Dickenson, *J. Chem. Soc. A*, 1971, 248.
29 F. M. Bickelhaupt, E. J. Baerends, N. M. M. Nibbering and T. Ziegler, *J. Am. Chem. Soc.*, 1993, **115**, 9160.
30 C. Clavero, M. Duran, A. Lledos, O. N. Ventura and J. Bertran, *J. Am. Chem. Soc.*, 1986, **108**, 923.
31 M. I. Menendez, J. A. Sordo and T. L. Sordo, *J. Comput. Chem.*, 1995, **16**, 659.
32 M. I. Menendez, J. A. Sordo and T. L. Sordo, *J. Mol. Struct. THEOCHEM*, 1996, **371**, 91.
33 B. S. Jursic, *J. Mol. Struct. THEOCHEM*, 1998, **434**, 37.
34 L. B. Harding, H. B. Schlegel, R. Krishnan and J. A. Pople, *J. Phys. Chem.*, 1980, **84**, 3394.
35 S. Nagase and T. Kudo, *J. Chem. Soc., Chem. Commun.*, 1983, 363.
36 S. Yamabe, T. Minato and S. Inagaki, *J. Chem. Soc. Chem. Commun.*, 1988, 532.
37 Experimental evidence indicates that the reaction does not proceed *via* a cyclic transition state, see ref. 38.
38 (*a*) J. B. Anderson, *Int. J. Quantum. Chem.*, 1979, **15**, 109; (*b*) P. Havel, P. Cársky and R. Zahradník, *Theoret. Chim. Acta*, 1979, **53**, 1; (*c*) N. J. Brown and D. M. Silver, *J. Chem. Phys.*, 1980, **72**, 3869; (*d*) W. Gerhartz, R. D. Poshusta and J. Michl, *J. Am. Chem. Soc.*, 1977, **99**, 4263; (*e*) H. H. Huang and A. H. Pakiari, *Int. J. Quantum. Chem.*, 1977, **12**, 593.
39 M. Page and J. W. J. McIver, *J. Chem. Phys.*, 1988, **88**, 922.
40 For reviews, see (*a*) K. Morokuma and S. Kato, in *Potential Energy Characteristics for Chemical Reactions*, ed. D. H. Truhlar, Plenum, New York, 1981, p. 243; (*b*) W. Miller, in *The Theory of Chemical Reaction Dynamics*, ed. D. C. Clar, Reidel, Dordrecht, 1986, p. 27; (*c*) D. Truhlar and B. Garrett, *Annu. Rev. Phys. Chem.*, 1986, **35**, 159; (*d*) D. Truhlar, R. Steckler and M. Gordon, *Chem. Rev.*, 1987, **87**, 217; (*e*) D. Truhlar, F. Brown, R. Steckler and A. Isaacson, in *The Theory of Chemical Reaction Dynamics*, ed. C. D. Clar, Reidel, Dordrecht, 1986, p. 285.
41 E. Kraka and T. H. Dunning, Jr., in *Advances in Molecular Electronic Structure Theory: The Calculation and Characterization of Molecular Potential Energy Surfaces*, ed. T. H. Dunning, JAI Press, Inc., Greenwich, 1990, p. 129.
42 For a recent review see D. Cremer, in *Encyclopedia of Computational Chemistry*, ed. P. v. R. Schleyer, N. L. Allinger, T. Clark, J. Gasteiger, P. A. Kollman, H. F. Schaefer III and P. R. Schreiner, Wiley, Chichester, 1998, vol. 3, p. 1706.
43 (*a*) P. Hohenberg and W. Kohn, *Phys. Rev.*, 1994, **136**, B864; (*b*) W. Kohn and L. Sham, *J. Phys. Rev.*, 1965, **140**, A1133; see also, for example, (*c*) R. G. Parr and W. Yang, *International Series of Monographs on Chemistry 16: Density-Functional Theory of Atoms and Molecules*, Oxford University Press, New York, 1989.
44 For a recent reviews see (*a*) J. Gauss, in *Encyclopedia of Computational Chemistry*, ed. P. v. R. Schleyer, N. L. Allinger, T. Clark, J. Gasteiger, P. A. Kollman, H. F. Schaefer III and P. R. Schreiner, Wiley, Chichester, 1998, vol. 1, p. 615; (*b*) T. D. Crawford and H. F. Schaefer III, in *Reviews in Computational Chemistry*, ed. K. B. Lipkowitz, D. B. Boyd, Wiley-VCH, Weinheim, 2000, vol. 14, p. 33.
45 K. Raghavachari, G. W. Trucks, J. A. Pople and M. Head-Gordon, *Chem. Phys. Lett.*, 1989, **157**, 479.
46 P. C. Hariharan and J. A. Pople, *Theoret. Chim. Acta*, 1973, **28**, 213.
47 R. Krishnan, M. Frisch and J. A. Pople, *J. Chem. Phys.*, 1980, **72**, 4244.
48 T. H. Dunning, Jr., *J. Chem. Phys.*, 1989, **90**, 1007.
49 (*a*) A. D. Becke, *J. Chem. Phys.*, 1993, **98**, 5648; see also (*b*) J. P. Stevens, F. J. Devlin, C. F. Chablowski and M. J. Frisch, *J. Phys. Chem.*, 1994, **98**, 11623.
50 See, *e.g.*, J. Baker, M. Muir, J. Andzelm and A. Schreiner, in *Chemical Applications of Density Functional Theory*, ACS Symposium Series 629, ed. B. B. Laird, R. B. Ross and T. Ziegler, American Chemical Society, Washington, DC, 1996, p. 342.
51 L. A. Curtiss, K. Raghavachari, G. W. Trucks and J. A. Pople, *J. Chem. Phys.*, 1991, **94**, 7221.
52 N. R. Kestner and J. E. Comariza, in *Reviews in Computational Chemistry*, ed. K. B. Lipkowitz and D. B. Boyd, Wiley-VCH, New York, 1999, vol. 13, p. 99.
53 F. Boys and F. Bernardi, *Mol. Phys.*, 1970, **19**, 553.
54 (*a*) *NIST Standard Reference Database 25*, *Version 2.02*, National Institute of Standards and Technology, Gaithersburg, MD, USA, 1994; (*b*) J. D. Cox and G. Pilcher, *Thermochemistry of Organic and Organometallic Compounds*, Academic Press, London, 1970.

55 Z. Konkoli, D. Cremer and E. Kraka, *J. Comput. Chem.*, 1997, **18**, 1282.
56 E. Kraka, J. Gauss and D. Cremer, *J. Mol. Struct. THEOCHEM*, 1991, **234**, 95.
57 E. Kraka, J. Gräfenstein, J. Gauss, Y. He, F. Reichel, L. Olsson, Z. Konkoli, Z. He and D. Cremer, COLOGNE2000, Univeristy of Göteborg, 2000.
58 M. J. Frisch, G. W. Trucks, H. B. Schlegel, G. E. Scuseria, M. A. Robb, J. R. Cheeseman, V. G. Zakrzewski, J. A. Montgomery, Jr., R. E. Stratmann, J. C. Burant, S. Dapprich, J. M. Millam, A. D. Daniels, K. N. Kudin, M. C. Strain, O. Farkas, J. Tomasi, V. Barone, M. Cossi, R. Cammi, B. Mennucci, C. Pomelli, C. Adamo, S. Clifford, J. Ochterski, G. A. Petersson, P. Y. Ayala, Q. Cui, K. Morokuma, D. K. Malick, A. D. Rabuck, K. Raghavachari, J. B. Foresman, J. Cioslowski, J. V. Ortiz, B. B. Stefanov, G. Liu, A. Liashenko, P. Piskorz, I. Komaromi, R. Gomperts, R. L. Martin, D. J. Fox, T. Keith, M. A. AlLaham, C. Y. Peng, A. Nanayakkara, C. Gonzalez, M. Challacombe, P. M. W. Gill, B. Johnson, W. Chen, M. W. Wong, J. J. Andres, M. HeadGordon, E. S. Replogle and J. A. Pople, GAUSSIAN 98, Revision A.5, Gaussian, Inc., Pittsburgh, PA, 1998.
59 (*a*) J. F. Stanton, J. Gauss, J. D. Watts, W. J. Lauderdale and R. J. Bartlett, *ACES II*, Quantum Theory Project, University of Florida, 1992; (*b*) J. F. Stanton, J. Gauss, J. D. Watts, W. J. Lauderdale and R. J. Bartlett, *Int. J. Quantum. Chem. Symp.*, 1992, **26**, 879.
60 (*a*) R. J. Berry, C. J. Ehlers, D. R. Burgess, Jr., M. R. Zachariah, M. R. Nyden and M. Schwartz, *J. Mol. Struct. THEOCHEM*, 1998, **422**, 89; (*b*) T. Yamada, T. H. Lay and J. W. Bozzelli, *J. Phys. Chem. A*, 1998, **102**, 7286.
61 *CRC Handbook of Chemistry and Physics on CDROM, 2000 Version*, ed. D. R. Lide, CRC Press, Boca Raton, FL.
62 See, *e.g.*, (*a*) D. D. Shillady and C. Trindle, *Int. J. Quantum. Chem.*, 1972, **6**, 187; (*b*) C. Glidewell, *J. Mol. Struct.*, 1980, **67**, 121.